Optical Materials EXPRESS

Mid-infrared emission properties of erbium-doped fluorite-type crystals

SIMONE NORMANI,[1] PAVEL LOIKO,[1] LIZA BASYROVA,[1] ABDELMJID BENAYAD,[1] ALAIN BRAUD,[1] ELENA DUNINA,[2] LIUDMILA FOMICHEVA,[3] ALEXEY KORNIENKO,[2] AMMAR HIDEUR,[4] AND PATRICE CAMY[1,*]

[1] *Centre de Recherche sur les Ions, les Matériaux et la Photonique (CIMAP), UMR 6252 CEA-CNRS-ENSICAEN, Université de Caen Normandie, 6 Boulevard Maréchal Juin, 14050 Caen Cedex 4, France*
[2] *Vitebsk State Technological University, 210035 Vitebsk, Belarus*
[3] *Belarusian State University of Informatics and Radioelectronics, 6 Brovka St., 220027, Minsk, Belarus*
[4] *CORIA UMR6614, CNRS-INSA-Université de Rouen, Normandie Université, Avenue de l'université, BP. 12, 76801 Saint Etienne du Rouvray, France*
[*] *patrice.camy@ensicaen.fr*

Abstract: We report on a comparative study of the spectroscopic properties and mid-infrared laser performance of five 5 at.% Er^{3+}-doped fluorite-type crystals MF_2, including parent compounds CaF_2, SrF_2, BaF_2, and solid-solution ("mixed") ones $(Ca,Sr)F_2$ and $(Sr,Ba)F_2$. In the M = Ca → Sr → Ba series, the host matrix phonon energy decreases, the absorption and mid-infrared emission spectra of Er^{3+} become narrower and more structured, and the luminescence lifetimes of the $^4I_{11/2}$ and $^4I_{13/2}$ Er^{3+} manifolds increase. The Er^{3+} transition probabilities were calculated using the Judd-Ofelt theory. In the "mixed" compounds, the Er^{3+} ions tend to reside in the larger / heavier cation environment. The low-temperature (12 K) spectroscopy evidences the presence of a single type of clusters at this doping level; the crystal-field splitting for Er^{3+} ions in clusters was determined. Continuous-wave low-threshold laser operation at ~2.8 µm (the $^4I_{11/2} \rightarrow {}^4I_{13/2}$ transition) was achieved with all five Er^{3+}:MF_2 crystals. The maximum achieved laser slope efficiency was 37.9% (Er^{3+}:CaF_2), 23.5% (Er^{3+}:SrF_2) and 17.2% (Er^{3+}:BaF_2).

1. Introduction

Calcium fluoride (CaF_2, also known as fluorite in the mineral form) is a well-known laser host material for doping with trivalent rare-earth ions (RE^{3+}) [1–3]. Undoped CaF_2 features good thermal properties (high thermal conductivity and isotropic thermal expansion), low phonon energy, low refractive index and broadband transparency. It also exhibits a unique tendency for strong RE^{3+} ion clustering even at moderate doping concentrations (>0.1 at.%), leading to inhomogeneously broadened spectral bands [4–6]. As a result, the absorption and emission spectra of RE^{3+} ions in CaF_2 greatly resemble those in fluoride glasses being almost structureless and very broad. Such a "glassy-like" spectroscopic behavior is very appealing for broadband wavelength tuning [7,8] and generation of ultrashort pulses in mode-locked lasers [9,10]. The energy-transfer processes among the neighboring RE^{3+} ions (nonradiative energy-transfer, cross-relaxation, and energy-transfer upconversion) are greatly promoted in clusters [11]. This can be used for boosting the efficiency of certain laser transitions of RE^{3+} ions. CaF_2 is a low-melting-point compound. Its growth is well-developed, e.g., by the Czochralski or Bridgman-Stockbarger methods.

CaF_2 belongs to the family of divalent metal fluorides, MF_2 (where M = Ca, Sr, Ba, Cd, or Pb) [12–15]. These materials all belong to the cubic class (sp. gr. $Fm3^{-}m$, fluorite-type structure). The M^{2+} and F^{-} are located at face-centered cubic lattice points and tetrahedral voids, respectively. Compared to CaF_2, other MF_2 crystals are less studied for RE^{3+} doping

#482402 https://doi.org/10.1364/OME.482402
Journal © 2023 Received 1 Dec 2022; revised 24 Feb 2023; accepted 26 Feb 2023; published 2 Jun 2023

but they are also attractive as laser host media as they benefit from either a lower melting point, or better thermal properties, or lower phonon energies. Fluorite-type crystals can also form substitutional solid-solutions $(M1_{1-x}M2_x)F_2$ for the entire range of $0 < x < 1$ [16–18]. For such "mixed" compositions, the melting point is expected to decrease further as compared to the parent compounds [19,20]. An additional spectral broadening is also expected due to the compositional disorder. The growth and laser operation of some RE^{3+}-doped "mixed" fluorite-type crystals were reported mainly focusing on $(Ca,Sr)F_2$ [21–23].

Erbium ions (Er^{3+}) are of interest for generation of mid-infrared radiation at ~2.8 µm [24,25] according to the $^4I_{11/2} \rightarrow {}^4I_{13/2}$ transition, Fig. 1. The low-phonon-energy behavior of MF_2 crystals and the tendency for strong ion clustering promoting the energy-transfer upconversion stimulate the interest in the development of mid-infrared $Er^{3+}:MF_2$ lasers. Labbe *et al.* first reported on a mid-infrared 5 at.% $Er^{3+}:CaF_2$ laser delivering 80 mW at 2.80 µm with a slope efficiency of 30% and a small laser threshold of 23 mW [1]. Basyrova *et al.* demonstrated power scaling of a similar laser generating 0.83 W at 2.80 µm with a slightly higher slope efficiency of 31.6% [26]. In these studies, high-brightness laser pumping was implemented. Further power scaling was achieved using commercial InGaAs diode lasers as pump sources. Zong *et al.* developed a diode-pumped 1.7 at.% $Er^{3+}:CaF_2$ laser generating 2.32 W at 2.76 µm at the expense of a lower slope efficiency of 21.2% [27]. So far, $Er^{3+}:CaF_2$ [26,27], $Er^{3+}:SrF_2$ [28] and $Er^{3+}:(Ca,Sr)F_2$ [23] crystals have been studied for mid-infrared lasers. Note that $Er^{3+}:CaF_2$ can also be obtained in the form of transparent ceramics. Šulc *et al.* reported on a pulsed diode-pumped 5 at.% $Er^{3+}:CaF_2$ ceramic laser with a broad tuning range of 2687–2805 nm (118 nm) [29].

Despite the existence of multiple studies for several $Er^{3+}:MF_2$ crystal compositions, their spectroscopic and mid-infrared laser properties have not been directly compared so far. In the present work, we report on a comparative study of mid-infrared emission properties of five fluorite-type Er^{3+}-doped MF_2 crystals, including parent and solid-solution compounds.

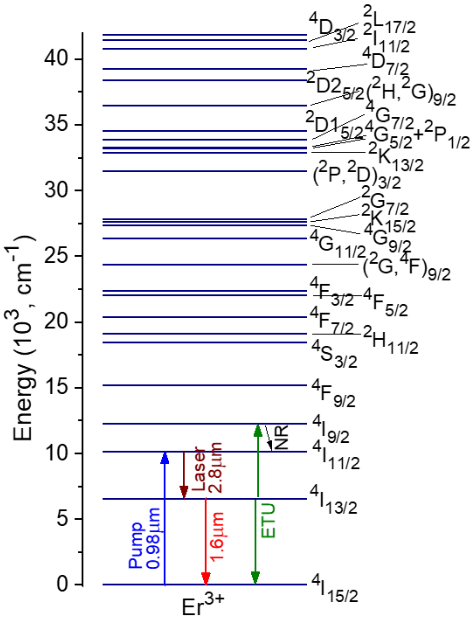

Fig. 1. Energy level scheme of Er^{3+} ions showing all the manifolds assigned in the absorption spectra of $Er^{3+}:MF_2$ crystals, pump and laser transitions, ETU – energy-transfer upconversion.

2. Crystal growth

The MF_2 crystals (M = Ca, Sr, Ba) melt congruently at relatively low temperatures and they can be grown by the Bridgman-Stockbarger or Czochralski methods. The Er^{3+}:MF_2 crystals were grown by the Bridgman method using graphite crucibles (Φ7-8 mm, height: 40 mm). The MF_2 (M = Ca, Sr, Ba) powders (purity: 4N, Sigma-Aldrich) and ErF_3 powder obtained by fluorination of the Er_2O_3 precursor (4N, Alfa Aesar). Five compositions were tested: M = Ca, Sr, Ba, $Ca_{0.5}Sr_{0.5}$ and $Sr_{0.5}Ba_{0.5}$. The doping level was 5 at.% Er^{3+} (with respect to M^{2+} cations). The optical quality and spectroscopic properties of RE^{3+}-doped MF_2 crystals are sensitive to even small pollution of oxygen / water in the growth chamber as they can lead to the presence of oxygen-assisted sites for the dopant ions or even formation of a translucent oxyfluoride phase. To avoid that, the growth chamber was sealed to vacuum ($<10^{-5}$ mbar) and refilled with a mixture of Ar + CF_4 gases. The starting reagents were well mixed and placed into the crucible which was then heated slightly above (~30-50 °C) the melting point and the solution was homogenized for 3-4 hours (h). The growth was ensured by a vertical translation of the crucible in a vertical temperature gradient of 30-40 °C/cm. After the growth was completed, the crystals were cooled down to room temperature (20 °C) within 48 h.

For the “mixed” crystals, the melting point is reduced as compared to those of the parent compounds. E.g., for Er^{3+}:(Ca,Sr)F_2 and Er^{3+}:(Sr,Ba)F_2, it is $T_f = 1373$ °C and 1315 °C, respectively (compare with 1477 °C, 1418 °C and 1386 °C for SrF_2, CaF_2 and BaF_2, respectively).

The as-grown Er^{3+}:MF_2 crystals with a cylindrical shape (Φ7-8 mm, length: 35 - 40 mm) were transparent and rose-colored due to the Er^{3+} doping, Fig. 2(a). Samples for spectroscopic and laser studies were cut from the central part of the cylindrical barrels with a thickness of 6-7 mm and then polished to laser-grade quality, Fig. 2(b).

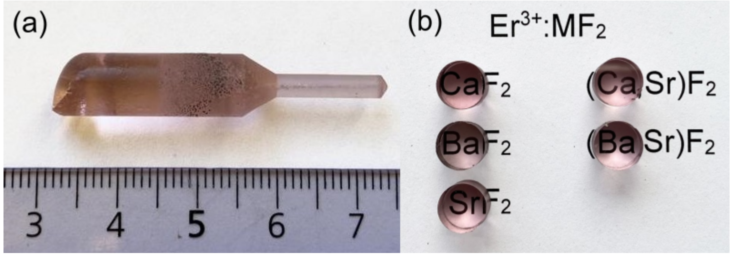

Fig. 2. Photographs of Er^{3+}:MF_2 crystals: (a) an as-grown Er^{3+}:CaF_2 crystal boule; (b) cut and polished Er^{3+}:MF_2 samples.

3. Raman spectra

The Raman spectra of Er^{3+}:MF_2 crystals, Fig. 3(a), were measured using a confocal microscope (InVia, Renishaw) equipped with a × 50 Leica objective and an Ar^+ ion laser (457 nm). Fluorite-type crystals have O_h symmetry and a triatomic unit cell thus exhibiting only one Raman-active mode at the center of the Brillouin zone having a T_{2g} symmetry [30]. Indeed, the Raman spectra of all the studied Er^{3+}:MF_2 crystals contain a single intense peak assigned to this vibration. Frequently, MF_2 crystals may exhibit additional broad Raman bands in the spectral range of 100–600 cm^{-1} owing to structure defects (interstitial / vacant anion sites) [30, 31]. Such a behavior is not observed in our crystals.

For Er^{3+}:CaF_2, Er^{3+}:SrF_2 and Er^{3+}:BaF_2 crystals, the peak frequency of the Raman mode and its linewidth (FWHM) are 321 / 11.0 cm^{-1}, 285 / 10.2 cm^{-1} and 242 / 12.0 cm^{-1}, respectively. Thus, the latter compound is the most favorable one in terms of low-phonon-energy behavior. For the “mixed” compositions, the Raman peak broadens and is reduced in intensity and the peak

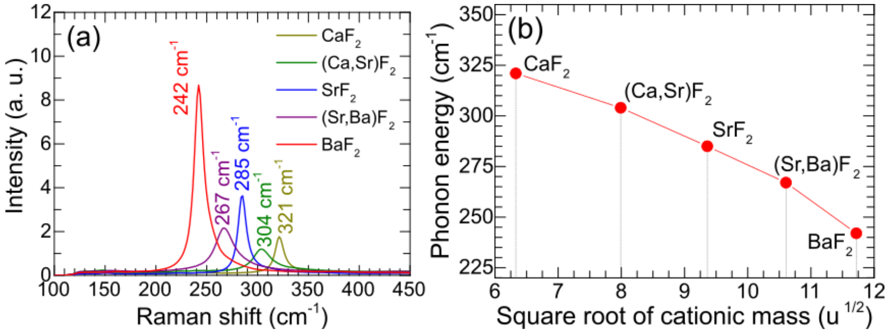

Fig. 3. Raman spectroscopy of Er^{3+}:MF_2 crystals: (a) Raman spectra, $\lambda_{exc} = 457\,cm^{-1}$, *numbers* – peak frequencies; (b) phonon energy vs. the square root of the average cationic mass.

position takes an intermediate place between those for the corresponding parent compounds, indicating an even distribution of the host-forming cations throughout the structure (a formation of a substitutional solid-solution) [32]. E.g., for Er^{3+}:(Ca,Sr)F_2, the peak Raman frequency is 304 cm^{-1} and the peak linewidth is 25.9 cm^{-1}.

The phonon energy of Er^{3+}:MF_2 decreased monotonically with increasing the cationic mass in agreement with the classical approach, $\nu = (1/2\pi)(k/\mu)^{1/2}$, where k is the force constant and μ is the reduced mass of the M – F system [33].

4. Optical spectroscopy

4.1. Optical absorption

The absorption spectra of Er^{3+} ions were measured using a spectrophotometer (Lambda 1050, Perkin Elmer). They are shown in Fig. 4. Here, the assignment of Er^{3+} transitions is according to Carnall *et al.* [34]. The absorption spectra for both parent and "mixed" Er^{3+}:MF_2 crystals are smooth and broad owing to inhomogeneous spectral broadening caused by a strong ion clustering. In the series M = Ca → Sr → Ba, the complexity and diversity of RE^{3+} ion clusters in MF_2 crystals decrease leading to more intense and structured absorption bands which also exhibit a slight blue-shift [12]. Indeed, for the $^4I_{15/2} \rightarrow {}^4I_{11/2}$ transition, which is used for pumping mid-infrared erbium lasers, the peak absorption cross-section, σ_{abs}, varies from 2.77×10^{-21} cm^2 at 972.3 nm (Er^{3+}:BaF_2) to 2.59×10^{-21} cm^2 at 969.5 nm (Er^{3+}:SrF_2), and further to 2.22×10^{-21} cm^2 at 967.6 nm (Er^{3+}:CaF_2), while the corresponding absorption bandwidth is 12.9 nm (Er^{3+}:BaF_2), 16.9 nm (Er^{3+}:SrF_2), and 22.2 nm (Er^{3+}:CaF_2).

A close look at the absorption spectra of "mixed" crystals indicate that there is a great similarity between those of (Er^{3+}:(Ca,Sr)F_2 and Er^{3+}:SrF_2) and (Er^{3+}:(Sr,Ba)F_2 and Er^{3+}:BaF_2) ones, suggesting that the dopant ions in such solid-solution compounds tend to reside in clusters with a local surrounding predominantly composed of one of the two host-forming cations (namely, the heavier / larger one – Sr^{2+} or Ba^{2+}, respectively). This suggests that Er^{3+} clusters have a tendency to sit in the heavier-cation environment within the solid-solution ($M1_{1-x}M2_x$)F_2 crystals. A similar behavior was observed previously for clusters of Nd^{3+}/Lu^{3+} ions in "mixed" (Sr,Ba)F_2 crystals [35].

4.2. Judd-Ofelt analysis

The measured absorption spectra of Er^{3+} ions in the five studied MF_2 crystals were used to calculate the transition probabilities by means of the standard Judd-Ofelt (J-O) theory [36,37]. The reduced squared matrix elements $U^{(k)}$ (k = 2, 4, 6) were calculated using the free-ion

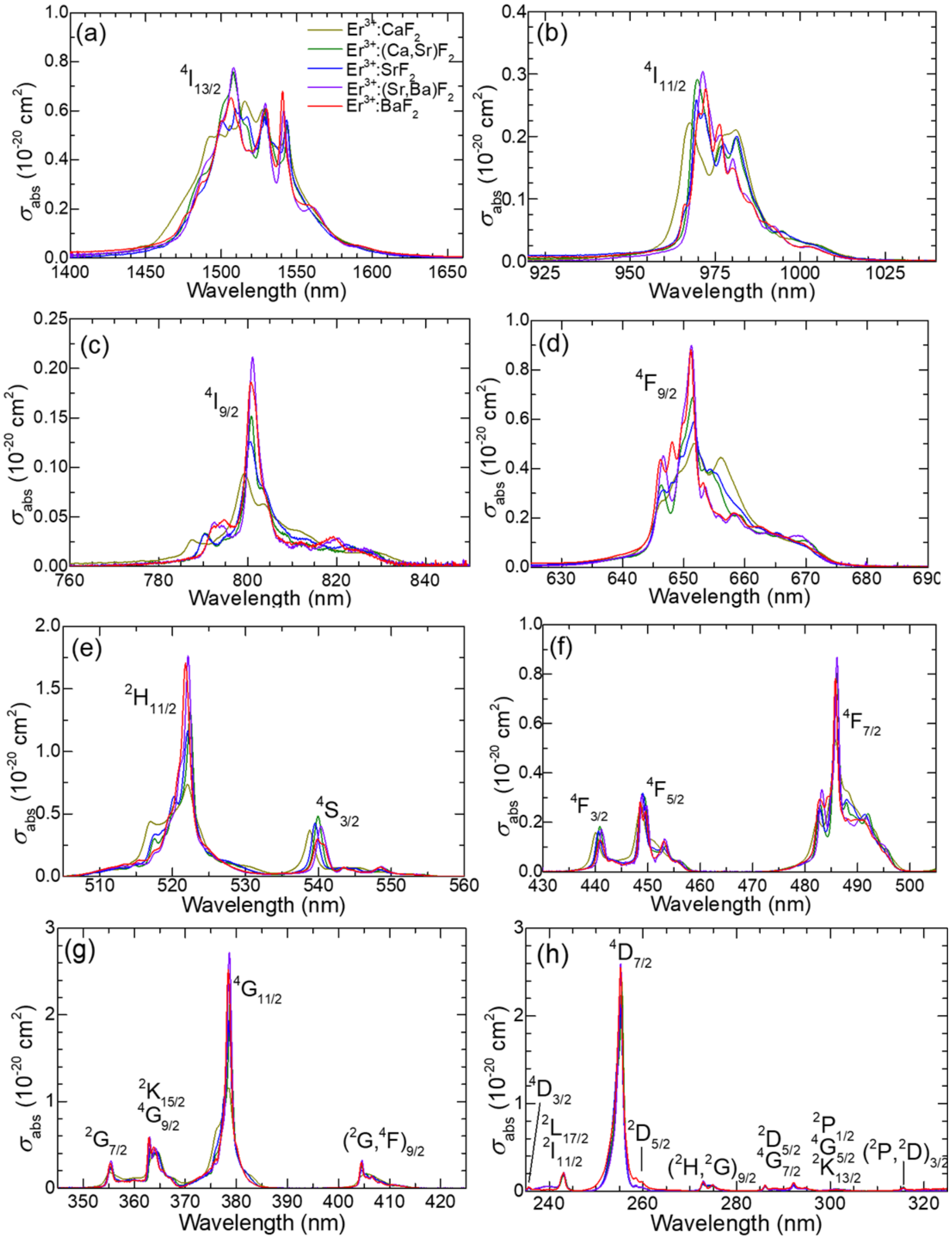

Fig. 4. (a-h) Absorption spectra of Er^{3+} ions in MF_2 crystals.

parameters from [38]. The magnetic dipole (MD) contributions to transition intensities (for $\Delta J = J - J' = 0, \pm 1$) were calculated within the Russell–Saunders approximation using Er^{3+} wave functions under the free-ion assumption.

Table 1 summarizes the experimental and calculated absorption oscillator strengths (f_{exp} and f_{calc}, respectively) for the three parent compounds, $Er^{3+}:CaF_2$, $Er^{3+}:SrF_2$ and $Er^{3+}:BaF_2$. There exists a direct relation between the absorption oscillator strength / integrated absorption cross-section and the radiative lifetime of the excited-state (the principle of reciprocity, referring to Einstein coefficients). For Er^{3+} transitions from the ground-state ($^4I_{15/2}$) to the two lower-lying excited-states ($^4I_{13/2}$ and $^4I_{11/2}$), the f_{calc} value decreases in the M = Ca → Sr → Ba series, so that an opposite tendency is expected for the radiative lifetimes of these two states. The root mean square (r.m.s.) deviation between the f_{exp} and f_{calc} values is relatively low for all the tested Er^{3+}:MF_2 crystals, lying in the range of 0.137–0.257.

Table 1. Absorption Oscillator Strengths[a] for Er^{3+} Ions in Parent MF_2 (M = Ca, Sr, Ba) Crystals

Transition $^4I_{15/2} \rightarrow {}^{2S+1}L_J$	Er^{3+}:CaF_2		Er^{3+}:SrF_2		Er^{3+}:BaF_2	
	f_{exp}, $\times 10^{-6}$	f_{calc}, J-O $\times 10^{-6}$	f_{exp}, $\times 10^{-6}$	f_{calc}, J-O $\times 10^{-6}$	f_{exp}, $\times 10^{-6}$	f_{calc}, J-O $\times 10^{-6}$
$^4I_{13/2}$	2.496	$1.643^{\mathrm{ED}} + 0.448^{\mathrm{MD}}$	2.129	$1.510^{\mathrm{ED}} + 0.448^{\mathrm{MD}}$	2.220	$1.404^{\mathrm{ED}} + 0.461^{\mathrm{MD}}$
$^4I_{11/2}$	0.714	0.693^{ED}	0.643	0.631^{ED}	0.598	0.592^{ED}
$^4I_{9/2}$	0.333	0.229^{ED}	0.328	0.283^{ED}	0.343	0.333^{ED}
$^4F_{9/2}$	2.264	2.139^{ED}	2.217	2.283^{ED}	2.265	2.406^{ED}
$^4S_{3/2} + {}^2H_{11/2}$	3.531	3.366^{ED}	3.422	3.544^{ED}	4.387	4.760^{ED}
$^4F_{7/2}$	2.141	2.454^{ED}	2.396	2.342^{ED}	2.205	2.236^{ED}
$^4F_{5/2} + {}^2F_{3/2}$	1.266	1.300^{ED}	1.114	1.173^{ED}	0.962	1.056^{ED}
$^2G_{9/2}$	0.898	0.970^{ED}	0.637	0.902^{ED}	0.603	0.840^{ED}
$^4G_{11/2} + {}^2K_{15/2} + {}^4G_{9/2} + {}^2G_{7/2}$	7.888	$7.917^{\mathrm{ED}} + 0.053^{\mathrm{MD}}$	8.585	$8.474^{\mathrm{ED}} + 0.053^{\mathrm{MD}}$	11.400	$11.168^{\mathrm{ED}} + 0.055^{\mathrm{MD}}$
r.m.s. dev.		*0.217*		*0.137*		*0.234*

[a] f_{exp} and f_{calc} - experimental and calculated absorption oscillator strengths, respectively, ED – electric dipole, MD – magnetic dipole.

The J-O (intensity) parameters Ω_2, Ω_4, Ω_6 for Er^{3+} ions in MF_2 crystals are listed in Table 2.

Table 2. Judd-Ofelt Parameters of Er^{3+} Ions in MF_2 Crystals

Host crystal	Ω_2, 10^{-20} cm^2	Ω_4, 10^{-20} cm^2	Ω_6, 10^{-20} cm^2
CaF_2	1.436	1.364	1.892
$(Ca,Sr)F_2$	1.244	1.483	1.720
SrF_2	1.477	1.701	1.701
$(Sr,Ba)F_2$	1.519	1.836	1.529
BaF_2	2.397	1.964	1.487

The determined J-O parameters were used to calculate the probabilities of spontaneous radiative transitions of Er^{3+} ions. In Table 3, we list the parameters relevant for mid-infrared laser operation, i.e., the radiative lifetimes τ_{rad} of the $^4I_{13/2}$ and $^4I_{11/2}$ states and the luminescence branching ratio $\beta_{JJ'}$ for the $^4I_{11/2} \rightarrow {}^4I_{13/2}$ transition. As expected, in the M = Ca → Sr → Ba series, the τ_{rad} values for the considered excited-states tend to increase from 7.09 / 6.53 ms (Er^{3+}:CaF_2) to 7.57 / 6.99 ms (Er^{3+}:SrF_2) and further to 7.52 / 7.11 ms (Er^{3+}:BaF_2). The considered $\beta_{JJ'}$ value is also higher for Sr^{2+} and Ba^{2+}-containing crystals.

4.3. Emission spectra and luminescence lifetimes

The luminescence spectra of Er^{3+} ions in the mid-infrared (the $^4I_{11/2} \rightarrow {}^4I_{13/2}$ transition) were measured using an optical spectrum analyzer (OSA, Yokogawa AQ6376) and a ZrF_4 fiber. The excitation source was a Ti:Sapphire laser tuned to ~970 nm. The OSA was purged with N_2 gas.

Table 3. Selected Probabilities[a] of Spontaneous Radiative Transitions of Er^{3+} in MF_2 crystals

Host crystal	$\tau_{rad}(^4I_{13/2})$, ms	$\tau_{rad}(^4I_{11/2})$, ms	$\beta_{JJ'}(^4I_{11/2} \longrightarrow {}^4I_{13/2})$, %
CaF_2	7.09	6.53	14.9
$(Ca,Sr)F_2$	7.64	7.06	15.8
SrF_2	7.57	6.99	16.0
$(Sr,Ba)F_2$	7.90	7.56	16.5
BaF_2	7.52	7.11	16.1

[a] τ_{rad} – radiative lifetime, $\beta_{JJ'}$ – luminescence branching ratio.

To remove the effect of the residual water vapor absorption in air, the set-up was calibrated using a 20 W quartz iodine lamp.

The stimulated-emission (SE) cross-sections, σ_{SE}, were calculated using the Füchtbauer-Ladenburg equation [39]:

$$\sigma_{SE}(\lambda) = \frac{\lambda^5}{8\pi{<}n{>}^2\tau_{rad}c}\frac{B(JJ')W'(\lambda)}{\int \lambda W'(\lambda)\mathrm{d}\lambda}, \tag{1}$$

where λ is the light wavelength, $<n>$ is the refractive index of the crystal at the mean emission wavelength, τ_{rad} corresponds to the $^4I_{11/2}$ state and $\beta_{JJ'}$ – to the $^4I_{11/2} \to {}^4I_{13/2}$ transition (cf. Table 3), c is the speed of light, and $W'(\lambda)$ is the measured luminescence spectrum corrected for the response of the set-up.

The SE cross-section spectra for Er^{3+} ions in MF_2 crystals are shown in Fig. 5. Similarly to the absorption spectra, a profound inhomogeneous broadening is observed for both the parent and "mixed" Er^{3+}:MF_2 crystals owing to the rare earth ion clustering. For all the studied crystals, the emission spectra are very broad extending from 2.55 to 3.05 µm and the main emission peak appears around 2.72 µm. Such a behavior is beneficial for broadly tunable and potentially mode-locked lasers. The spectra become more structured in the M = Ca → Sr → Ba series. Also for the solid-solution compounds, a great similarity between the emission spectra of (Er^{3+}:$(Ca,Sr)F_2$ and Er^{3+}:SrF_2) and (Er^{3+}:$(Sr,Ba)F_2$ and Er^{3+}:BaF_2) crystals is observed.

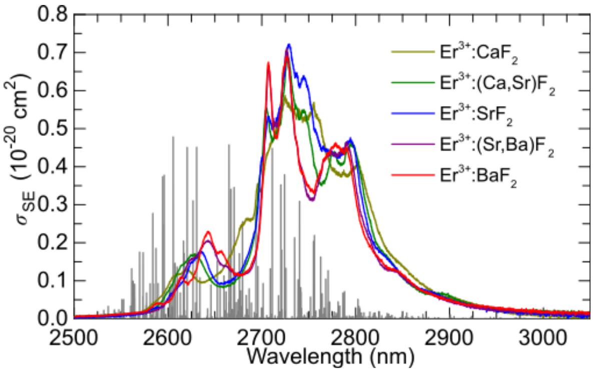

Fig. 5. Stimulated-emission (SE) cross-sections, σ_{SE}, for the $^4I_{11/2} \to {}^4I_{13/2}$ Er^{3+} transition in MF_2 crystals, corrected for the structured water vapor absorption in air (in *grey*, arb. units, according to the HITRAN database).

The highest SE cross-section is observed for Er^{3+}:SrF_2, $\sigma_{SE} = 7.19 \times 10^{-21}$ cm^2 at 2729 nm and at longer wavelengths, two other intense and broad peaks appear ($\sigma_{SE} = 6.38 \times 10^{-21}$ cm^2 at 2745 nm and 4.69×10^{-21} cm^2 at 2794 nm).

Luminescence decays were studied under resonant excitation using a ns optical parametric oscillator (Horizon, Continuum), a 1/4 m monochromator (Oriel 77200), an InGaAs detector and an 8 GHz oscilloscope (DSA70804B, Tektronix). To reduce the reabsorption (radiation trapping) effect on the measured kinetics, the samples were finely ground into powders. The measured luminescence decay curves from the $^4I_{13/2}$ and $^4I_{11/2}$ Er^{3+} states in the three parent crystals, CaF_2, SrF_2 and BaF_2, are shown in Fig. 6(a). They deviate from the single-exponential law (especially for $^4I_{13/2}$) owing to the strong ETU from these long-living states. Thus, the mean luminescence lifetimes $<\tau_{\text{lum}}> = \int t \cdot \mathrm{I}(t)\mathrm{d}t / \int I(t)\mathrm{d}t$ were determined.

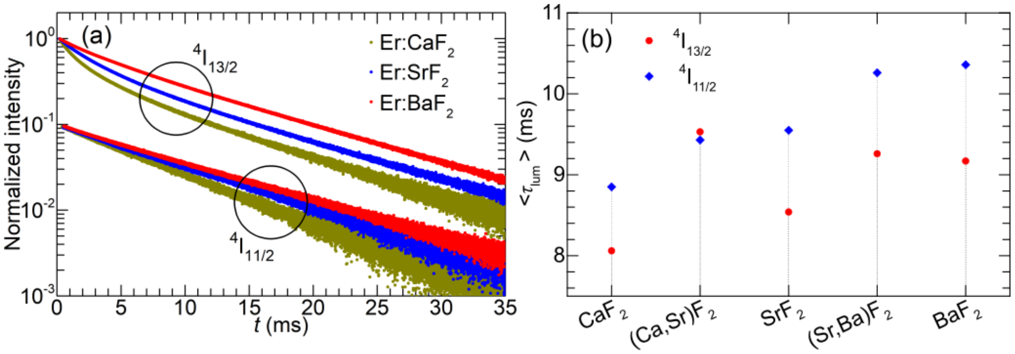

Fig. 6. Luminescence dynamics from the $^4I_{13/2}$ and $^4I_{11/2}$ Er^{3+} manifolds in MF_2 crystals: (a) luminescence decay curves under resonant excitation of Er^{3+} ions in CaF_2, SrF_2, and BaF_2, $\lambda_{\text{exc}} = 1.48$ µm, $\lambda_{\text{lum}} = 1.57$ µm (the $^4I_{13/2}$ state), $\lambda_{\text{exc}} = 0.97$ µm, $\lambda_{\text{lum}} = 1.01$ µm (the $^4I_{11/2}$ state); (b) mean luminescence lifetimes $<\tau_{\text{lum}}>$ as a function of the host composition.

The summary of the $<\tau_{\text{lum}}>$ values for the five studied Er^{3+}:MF_2 crystals is given in Fig. 6(b). With increasing the average radius / atomic mass of the M^{2+} host-forming cations (in the M = Ca → Sr → Ba series), and, accordingly, decreasing the phonon energy of the host matrix, both the $^4I_{13/2}$ and $^4I_{11/2}$ luminescence lifetimes tend to increase, from 8.06 / 8.85 ms (Er^{3+}:CaF_2) to 8.54 / 9.55 ms (Er^{3+}:SrF_2) and further to 9.17 / 10.36 ms (Er^{3+}:BaF_2). This behavior agrees with that for the calculated radiative lifetimes of these manifolds. The ratio of the upper-to-lower laser level lifetimes is favorable for all the studied crystals being weakly dependent on the host matrix composition. The long luminescence lifetime of the upper laser level for the mid-infrared transition ($^4I_{11/2}$) is a prerequisite for a low-threshold behavior.

Note that the measured luminescence lifetimes are slightly exceeding the radiative ones calculated using the J-O theory (cf. Table 3). One possible reason for that is the residual reabsorption effect within the Er^{3+} ion clusters. Table 4 summarizes the key spectroscopic properties of Erbium ions in fluorite-type crystals being relevant for mid-infrared laser operation.

4.4. Low-temperature spectroscopy

For low-temperature (LT, 12 K) absorption and luminescence studies, we have used an APD DE-202 closed-cycle cryo-cooler equipped with an APD HC 2 Helium vacuum cryo-compressor and a Laceshore 330 temperature controller. For absorption measurements, a 20 W quartz lamp with a calibrated spectral output was used. The spectra were measured using optical spectrum analyzers (Ando AQ6315A and Yokogawa AQ6375E). The luminescence was excited by a Ti:Sapphire laser tuned to ~800 nm.

The LT absorption and emission spectra are shown in Fig. 7 and Fig. 8, respectively. In each graph, we compare the spectrum of a "mixed" compound with those of both parent crystals. The LT absorption spectra were lotted versus the photon energy giving access to the splitting of the

$^4I_{13/2}$ and $^4I_{11/2}$ excited-states, while the LT emission spectra were plotted versus (E_{ZPL} – photon energy), where E_{ZPL} is the zero-phonon line (ZPL) energy giving access to the splitting of the ground-state $^4I_{15/2}$.

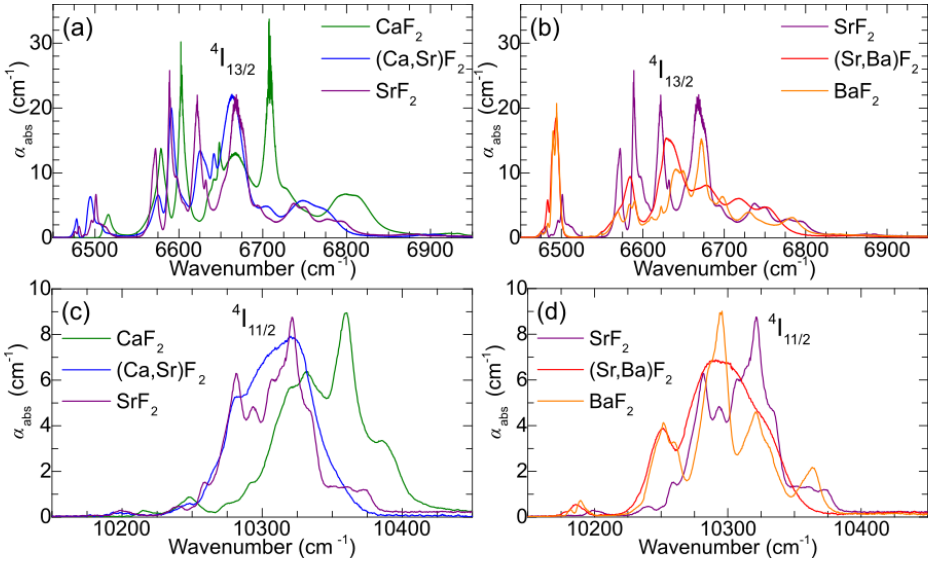

Fig. 7. (a-d) LT (12 K) absorption spectra of Er^{3+} ions in fluorite-type crystals: (a,b) the $^4I_{15/2} \rightarrow {}^4I_{13/2}$ transition; (c,d) $^4I_{15/2} \rightarrow {}^4I_{11/2}$ transition. α_{abs} – absorption coefficient.

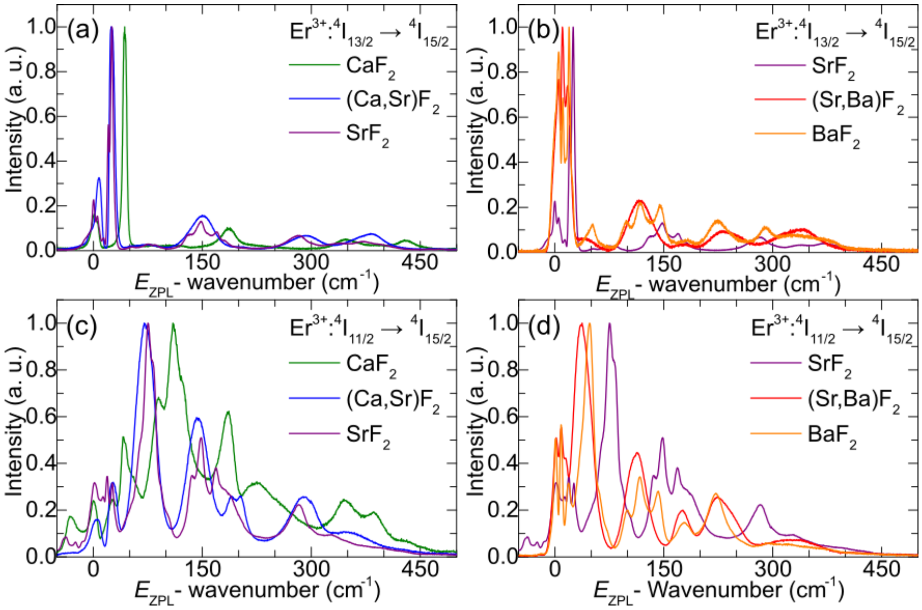

Fig. 8. (a-d) LT (12 K) luminescence spectra of Er^{3+} ions in fluorite-type crystals: (a,b) the $^4I_{13/2} \rightarrow {}^4I_{15/2}$ transition; (c,d) $^4I_{11/2} \rightarrow {}^4I_{15/2}$ transition. E_{ZPL} – zero-phonon-line energy.

By analyzing the spectra, several conclusions can be derived:

(i) The absorption and emission spectra of Er^{3+} ions in MF_2 crystals contain very broad bands even at 12 K indicating a significant inhomogeneous spectral broadening due to the rare-earth ion clustering. The spectra become more structured in the series M = Ca → Sr → Ba indicating smaller variety of cluster geometries;

(ii) The spectra of "mixed" fluorite-type crystals exhibit additional broadening as compared to the corresponding parent compounds due to the presence of two different host-forming cations. The spectra of such "mixed" crystals are more similar to those of the heavier-cation parent (e.g., $(Ca,Sr)F_2$ and SrF_2, $(Ba,Sr)F_2$ and BaF_2). This corroborates the observation made in Section 4.3, confirming that the majority of Er^{3+} ions tend to reside in the vicinity of heavier cations within "mixed" crystals;

(iii) The total Stark splitting of Er^{3+} multiplets in clusters in MF_2 crystals decreases in the M = Ca → Sr → Ba series, and the corresponding barycenter energies experience a progressive red-shift. The strength of the crystal-field is expected to be larger for smaller sites (shorter M – F and M - M distances, in our case) due to the stronger lattice distortion on the dopant ion. Indeed, the lattice constant increases in the series CaF_2 (5.45 Å) → SrF_2 (5.80 Å) → BaF_2 (6.20 Å).

Based on the LT absorption and emission spectra, the crystal-field splitting of the $^4I_{15/2}$, $^4I_{13/2}$ and $^4I_{11/2}$ multiplets of Er^{3+} ions forming clusters in the three parent MF_2 crystals (M = Ca, Sr, Ba), was determined, Table 5. The experimental Stark splitting of the $^4I_{11/2}$ and $^4I_{13/2}$ multiplets relevant for the 2.8 μm laser operation is also compared in Fig. 9. In the previous studies on site-selective spectroscopy of Er^{3+} ions in CaF_2 crystals grown under oxygen-free atmosphere, multiple possible sites were identified [40–42]. At very low doping levels (<0.05 at.%), the Er^{3+} ions are mostly isolated and are distributed over tetragonal (A, C_{4v}), trigonal (B, C_{3v}) and cubic (O_h) sites, depending on the relative position of the charge-compensating interstitial fluorine anion (F_i^-), namely at the (1,0,0) positions, at the (1,1,1) positions or sufficiently far from the dopant ion to exert negligible perturbation, respectively [40]. For higher doping levels of >0.1 at.%, the dopant ions form clusters of several types (assigned as C-sites, being close to dimers with a distorted C_{3v} symmetry, and D(1) and D(2) sites corresponding to larger agglomerates of Er^{3+} - F_i^- pairs).

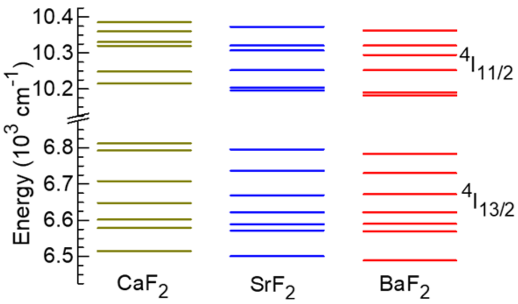

Fig. 9. Experimental Stark splitting of the $^4I_{11/2}$ and $^4I_{13/2}$ multiplets of Er^{3+} ions forming clusters in heavily doped Er^{3+}:MF_2 crystals.

For the studied heavily doped Er^{3+}:MF_2 crystals, we were not able to confirm the existence of two significantly different groups of ion clusters (D(1) and D(2)), as the LT emission spectra were almost independent on the excitation wavelength. Moreover, the bands in the LT spectra of ~5 at.% Er^{3+}-doped crystals (assigned to a single type of cluster D sites) experience an additional broadening and spectral shifts as compared to those in 0.1 at.% Er^{3+}-doped crystals (assigned to D(1) and D(2) sites). Thus, we assumed that almost all the Er^{3+} ions form large-scale agglomerates

Table 4. Spectroscopic Characteristics[a] of Er^{3+}:MF_2 Crystals

Parameter / Crystal	CaF_2	$(Ca,Sr)F_2$	SrF_2	$(Sr,Ba)F_2$	BaF_2
λ_{abs}, nm	967.6	969.7	969.5	971.4	972.3
σ_{abs}, 10^{-21} cm^2	2.22	2.91	2.59	3.04	2.77
λ_{em}, nm	2724.8	2727.6	2728.9	2726.6	2726.5
σ_{SE}, 10^{-21} cm^2	5.87	6.90	7.22	7.11	6.92
$<\tau_{lum}>$ ($^4I_{13/2}$), ms	8.06	9.53	8.54	9.26	9.17
$<\tau_{lum}>$ ($^4I_{11/2}$), ms	8.85	9.43	9.55	10.26	10.36

[a] λ_{abs}, λ_{em} – peak absorption / emission wavelengths, respectively, σ_{abs}, σ_{SE} – peak absorption / SE cross-sections, respectively, $<\tau_{lum}>$ - average luminescence lifetime.

Table 5. Crystal-Field Splitting of Selected Er^{3+} Multiplets in CaF_2, SrF_2, and BaF_2

Crystal	Er^{3+}	Sub-level / Energy (cm^{-1})							
	$^{2S+1}L_J$	1	2	3	4	5	6	7	8
CaF_2	$^4I_{15/2}$	0	42	90	110	186	228	346	387
	$^4I_{13/2}$	6516	6579	6602	6648	6708	6793	6812	
	$^4I_{11/2}$	10215	10248	10320	10331	10360	10386		
SrF_2	$^4I_{15/2}$	0	25	63	75	148	187	283	330
	$^4I_{13/2}$	6501	6572	6589	6622	6669	6737	6796	
	$^4I_{11/2}$	10196	10204	10282	10307	10321	10373		
BaF_2	$^4I_{15/2}$	0	18	34	48	117	142	222	293
	$^4I_{13/2}$	6489	6569	6590	6622	6672	6730	6784	
	$^4I_{11/2}$	10182	10190	10252	10295	10321	10363		

(D) with relatively close spectroscopic properties. Previously, it was suggested that for all the heavily doped MF_2 crystals (M = Ca, Sr, Ba) and their solid-solutions, such agglomerates most likely correspond to hexameric Y_6F_{37} superstructure units, which are nearly identical in volume and shape to the Ca_2F_{32} building blocks of the fluorite lattice and, consequently, they can be easily incorporated into this lattice while accommodating the excess F_i^- anions [5,43]. The local crystal-field symmetry for the dopant ions in Y_6F_{37} clusters is tetragonal (C_{4v}) [5].

The analysis of Table 2 confirms a decreased total Stark splitting of the multiplets and a red-shift of the zero-phonon line for Er^{3+} ions in the M = Ca → Sr → Ba series.

5. Laser operation

5.1. Laser setup

The scheme of the laser set-up is shown in Fig. 10. Cylindrical samples with a thickness of 6.53-6.99 mm and a diameter of ~7 mm were cut from the central parts of the as-grown Er^{3+}:MF_2 crystal boules. They were polished to laser-grade quality with good parallelism (<5’) from both sides and left uncoated. The laser elements were mounted on a passively cooled Cu-holder using a silver paint for better heat removal. A hemispherical cavity was implemented. It was formed by a flat pump mirror (PM) coated for high transmission (HT, $T = 85.7\%$) at 0.97 µm and high reflection (HR) at 2.6–3.0 µm, and a set of concave (radius of curvature: RoC = -100 mm) output couplers (OC) having a transmission T_{OC} in the range of 0.33% - 4% at 2.7–2.9 µm. The crystal was placed near the PM at a small distance (<1 mm). The geometrical cavity length was ~99 mm. The pump source was a CW Ti:Sapphire laser delivering up to 3.2 W at 0.97 µm (addressing the $^4I_{15/2} \rightarrow {}^4I_{11/2}$ Er^{3+} absorption peak) with a diffraction-limited beam quality ($M^2 \approx 1$). The pump radiation was focused into the laser crystal through the PM using an antireflection-coated achromatic lens (focal length: $f = 75$ mm) resulting in a pump spot size of $2w_P = 66 \pm 5$ µm. The pumping was in single pass. The residual (non-absorbed) pump after the OC was filtered out using a long-pass filter (Spectrogon, LP1400). The laser spectra were measured using a ZrF_4 fiber (Thorlabs) and a spectrum analyzer (Bristol, 771 series). The laser mode profile in the far-field was captured using a camera (Pyrocam IIIHR, Ophir-Spiricon).

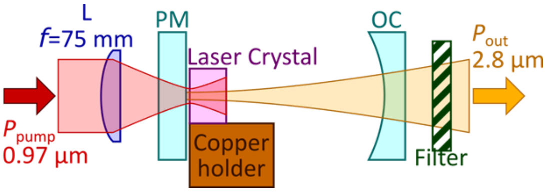

Fig. 10. Schematic of the laser setup: L – aspherical focusing lens; PM – flat pump mirror; OC – curved output coupler.

5.2. Laser performance

CW mid-infrared laser operation was obtained with all five studied Er^{3+}:MF_2 crystals. The best laser performance was achieved with the Er^{3+}:CaF_2 crystal: an output power of 702 mW was extracted at 2800 nm with a slope efficiency η of 37.9% (vs. the absorbed pump power) when using the output coupler with $T_{OC} = 4\%$, Fig. 11(a). With increasing output coupling from 0.33% to 4%, the laser threshold gradually increased from 16 mW to 60 mW. For Er^{3+}:CaF_2, the measured pump absorption reached 81.9%. The optical-to-optical efficiency (vs. the pump power incident on the crystal) η_{opt} was 31.0%. The output dependences were linear within the studied range of pump powers. Further power scaling was limited by the available pump. The achieved laser slope efficiency is slightly higher than the Stokes limit, $\eta_{St,L} = \lambda_P/\lambda_L = 34.6\%$, indicating the role of the ETU process $^4I_{13/2} + ^4I_{13/2} \rightarrow ^4I_{9/2} + ^4I_{15/2}$, cf. Figure 1, refilling the upper laser level and depopulating the intermediate $^4I_{13/2}$ state.

The typical emission spectra of the Er^{3+}:CaF_2 laser are shown in Fig. 11(b), measured well above the laser threshold. For small output coupling (<1%), laser emission at 2810 and 2814 nm was observed and for higher T_{OC}, the laser operated at 2800 nm. These wavelengths correspond to the long-wave emission peak of Er^{3+} ions in CaF_2 and match the transparency ranges between the structured water vapor absorption lines (cf. Figure 5). Note that due to strong resonant excited-state absorption from the terminal laser level with a non-negligible population, $^4I_{13/2} \rightarrow ^4I_{11/2}$, causing reabsorption of the laser photons, the $^4I_{11/2} \rightarrow ^4I_{13/2}$ Er^{3+} laser transition represents a quasi-three-level laser scheme with reabsorption, which explains the blue-shift of the laser spectra with increasing the output coupling.

The Er^{3+}:CaF_2 laser operated on the fundamental transverse mode, as confirmed by the measured $M^2 < 1.1$, and the beam profile in the far-field was nearly circular, see the inset in Fig. 11(a).

The output performance and laser spectra of five Er^{3+}:MF_2 crystals are directly compared in Fig. 11(c,d) using the same output coupling ($T_{OC} = 1.7\%$). The slope efficiency gradually decreased in the sequence Er^{3+}:CaF_2 → Er^{3+}:SrF_2 and Sr-containing crystals → Er^{3+}:BaF_2, while the laser threshold was in the range of 17–28 mW for all the crystals, being only slightly higher for Ba-containing ones. The laser emission occurred at 2792–2800 nm, except of Er^{3+}:SrF_2 for which the laser operated at shorter wavelengths, 2730 and 2747 nm. The output characteristics of mid-infrared Er^{3+}:MF_2 lasers are summarized in Table 6. More details about the 2.8 µm laser performance of Ba-containing crystals can be found in [44].

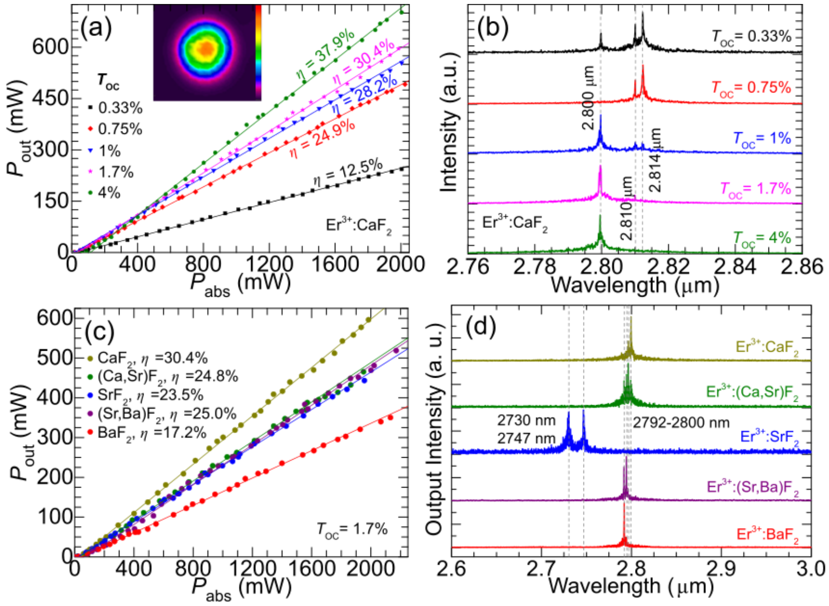

Fig. 11. Mid-infrared Er^{3+}:MF_2 lasers: (a,b) Er^{3+}:CaF_2 laser: (a) input-output dependences, η – slope efficiency, *inset* – far-field mode profile, P_{abs} ~1.5 W, T_{OC} = 1.7%; (b) typical laser spectra; (c,d) a comparison of (c) power transfer characteristics and (d) laser spectra for five Er^{3+}:MF_2 crystals, T_{OC} = 1.7%.

Table 6. Output Characteristics[a] of Mid-Infrared Er^{3+}:MF_2 Lasers (T_{OC} = 1.7%)

Parameter / Crystal	CaF_2	$(Ca,Sr)F_2$	SrF_2	$(Sr,Ba)F_2$	BaF_2
t, mm	6.81	6.99	6.53	6.99	6.66
λ_P, nm	967.8	969.7	969.5	971.4	971.2
η_{abs}, %	81.9	84.3	76.1	83.3	83.8
P_{out}, mW	596	466	443	519	350
λ_L, nm	2800	2796	2747	2794	2792
P_{th}, mW	20	17	20	28	26
η, %	30.4	24.8	23.5	25.0	17.2

[a] *t* – crystal thickness, λ_P - pump wavelength, η_{abs} – pump absorption under lasing conditions, P_{out} - output power, λ_L – laser wavelength, P_{th} – laser threshold, η – slope efficiency.

6. Conclusions

Fluorite-type Er^{3+}:MF_2 parent and solid-solution crystals feature low-phonon-energy behavior, very broad absorption and mid-infrared emission spectral bands, owing to the profound Er^{3+} ion clustering and long $^4I_{11/2}$ and $^4I_{13/2}$ luminescence lifetimes. As for the "mixed" compounds, their advantage is the lower melting points with respect to the corresponding parents. Considering the high thermal conductivity of these materials, the Er^{3+}:MF_2 crystals are very promising for the development of power-scalable and broadly tunable low-threshold mid-infrared lasers emitting at ~2.8 µm. Based on a detailed comparative spectroscopic study of five 5 at.% Er^{3+}:MF_2 fluorite-type crystals, including the parent compounds CaF_2, SrF_2, BaF_2, and "mixed" ones, (Ca,Sr)F_2 and (Sr,Ba)F_2, the following conclusions are derived:

(i) The phonon energy of Er^{3+}:MF_2 crystals monotonously decreases with the square root of the M^{2+} cationic mass, from 321 cm^{-1} (Er^{3+}:CaF_2) to 242 cm^{-1} (Er^{3+}:BaF_2). Such a low-phonon energy behavior is a prerequisite for almost vanishing multiphonon non-radiative path from both the $^4I_{11/2}$ and $^4I_{13/2}$ Er^{3+} manifolds, as confirmed by the luminescence decay studies and the Judd-Ofelt analysis yielding the radiative lifetimes;

(ii) In the M = Ca ⟶ Sr ⟶ Ba series, the absorption and mid-infrared emission spectra gradually become narrower and more structured, which is linked to the decreasing complexity of Er^{3+} clusters, and the luminescence lifetimes of the $^4I_{13/2}$ / $^4I_{11/2}$ Er^{3+} manifolds increase, from 8.06 / 8.85 ms (Er^{3+}:CaF_2) to 9.17 / 10.36 ms (Er^{3+}:BaF_2) because of a decrease in the crystal field strength. The observed ratio of the upper-to-lower laser level lifetimes and their values are favorable for low-threshold mid-infrared laser operation;

(iii) The Er^{3+} ions in "mixed" crystals tend to reside in a local environment predominantly composed of the larger / heavier M^{2+} cations, leading to a great similarity between the spectra of Er^{3+}:SrF_2 and Er^{3+}:(Ca,Sr)F_2, Er^{3+}:BaF_2 and Er^{3+}:(Sr,Ba)F_2. At LT, the spectra of Er^{3+} ions in solid-solution crystals exhibit a notable inhomogeneous broadening;

(iv) For the doping level of 5 at.% Er^{3+} in MF_2 crystals, the LT spectroscopy reveals the existence of a single class of Er^{3+} clusters with rather close absorption / emission properties (D centers), contrary to crystals with low doping levels subject to ion clustering of various nature (D(1) and D(2)).

In the present work, we employed high-brightness pumping to reveal the potential of Er^{3+}:MF_2 crystals for efficient lasing at ~2.8 µm. Further power scaling is envisioned by using powerful InGaAs laser diodes as pump sources which is feasible owing to the good thermal properties of these compounds. Further improvement of the slope efficiency, especially for Sr and Ba-containing crystals should involve an optimization of the Er^{3+} doping level for boosting the ETU efficiency. One hypothesis here is that a reduction in the cluster complexity may lead to weaker energy-transfer processes. Another idea is the Er^{3+},Pr^{3+} codoping for quenching the metastable Er^{3+} lower-laser level ($^4I_{13/2}$).

Funding. Contrat de Plan État-Région(CPER) de Normandie 2021-2027; Région Normandie (Chair of Excellence project, RELANCE); Agence Nationale de la Recherche (ANR-19-CE08-0028, SPLENDID2).

Disclosures. The authors declare no conflicts of interest.

Data availability. Data underlying the results presented in this paper are not publicly available at this time but may be obtained from the authors upon reasonable request.

References

1. C. Labbe, J. L. Doualan, P. Camy, R. Moncorgé, and M. Thuau, "The 2.8 µm laser properties of Er^{3+} doped CaF_2 crystals," Opt. Commun. **209**(1-3), 193–199 (2002).

2. F. Druon, S. Ricaud, D. N. Papadopoulos, A. Pellegrina, P. Camy, J. L. Doualan, R. Moncorgé, A. Courjaud, E. Mottay, and P. Georges, "On Yb:CaF_2 and Yb:SrF_2: review of spectroscopic and thermal properties and their impact on femtosecond and high power laser performance," Opt. Mater. Express **1**(3), 489–502 (2011).
3. P. Camy, J. L. Doualan, S. Renard, A. Braud, V. Ménard, and R. Moncorgé, "Tm^{3+}: CaF_2 for 1.9 µm laser operation," Opt. Commun. **236**(4-6), 395–402 (2004).
4. V. Petit, P. Camy, J.-L. Doualan, X. Portier, and R. Moncorgé, "Spectroscopy of Yb^{3+}:CaF_2: from isolated centers to clusters," Phys. Rev. B **78**(8), 085131 (2008).
5. S. A. Kazanskii and A. I. Ryskin, "Group-III Ion Clusters in Activated Fluorite-Like Crystals," Phys. Solid State **44**(8), 1415–1425 (2002).
6. B. Lacroix, C. Genevois, J. L. Doualan, G. Brasse, A. Braud, P. Ruterana, P. Camy, E. Talbot, R. Moncorgé, and J. Margerie, "Direct imaging of rare-earth ion clusters in Yb:CaF_2," Phys. Rev. B **90**(12), 125124 (2014).
7. V. Petit, J. L. Doualan, P. Camy, V. Ménard, and R. Moncorgé, "CW and tunable laser operation of Yb^{3+} doped CaF_2," Appl. Phys. B **78**(6), 681–684 (2004).
8. R. Thouroude, A. Tyazhev, A. Hideur, P. Loiko, P. Camy, J. L. Doualan, H. Gilles, and M. Laroche, "Widely tunable in-band-pumped Tm:CaF_2 laser," Opt. Lett. **45**(16), 4511–4514 (2020).
9. G. Machinet, P. Sevillano, F. Guichard, R. Dubrasquet, P. Camy, J. L. Doualan, R. Moncorgé, P. Georges, F. Druon, D. Descamps, and E. Cormier, "High-brightness fiber laser-pumped 68 fs-2.3 W Kerr-lens mode-locked Yb:CaF_2 oscillator," Opt. Lett. **38**(20), 4008–4010 (2013).
10. A. Lucca, G. Debourg, M. Jacquemet, F. Druon, F. Balembois, P. Georges, P. Camy, J. L. Doualan, and R. Moncorge, "High-power diode-pumped Yb^{3+}:CaF_2 femtosecond laser," Opt. Lett. **29**(23), 2767–2769 (2004).
11. P. Loiko, A. Braud, L. Guillemot, J.L. Doualan, A. Benayad, and P. Camy, "Cross-relaxation and ion clustering in Tm3+:CaF2 crystals," Proc. SPIE **11357**, 23 (2020).
12. P. Camy, J. L. Doualan, A. Benayad, M. Von Edlinger, V. Ménard, and R. Moncorgé, "Comparative spectroscopic and laser properties of Yb^{3+}-doped CaF_2, SrF_2 and BaF_2 single crystals," Appl. Phys. B **89**(4), 539–542 (2007).
13. S. Bordj, H. Satha, A. Barros, D. Zambon, J. P. Jouart, M. Diaf, and M. and , and R. Mahiou, "Spectroscopic characterization by up conversion of Ho^{3+}/Yb^{3+} codoped CdF_2 single crystal," Opt. Mater. (Amsterdam, Neth.) **118**, 111249 (2021).
14. M. Zhou, P. Zhang, X. Niu, J. Liao, Q. Chen, S. Zhu, Y. Hang, Q. Yang, H. Yin, Z. Li, and Z. Chen, "Ultra-broadband and enhanced near-infrared emission in Bi/Er co-doped PbF_2 laser crystal," J. Alloys Compd. **895**, 162704 (2022).
15. W. Z. Xue, Z. L. Lin, H. J. Zeng, G. Zhang, P. Loiko, L. Basyrova, A. Benayad, P. Camy, V. Petrov, X. Mateos, L. Wang, and W. Chen, "Diode-pumped mode-locked Yb:BaF_2 laser," Opt. Express **30**(9), 15807–15818 (2022).
16. S. V. Kuznetsov, V. A. Konyushkin, A. N. Nakladov, E. V. Chernova, P. A. Popov, A. A. Pynenkov, K. N. Nishchev, and P. P. Fedorov, "Thermophysical properties of single crystals of CaF_2–SrF_2–RF_3 (R = Ho, Pr) fluorite solid solutions," Inorg. Mater. **56**(9), 975–981 (2020).
17. P. P. Fedorov, I. I. Buchinskaya, N. A. Ivanovskaya, V. V. Konovalova, S. V. Lavrishchev, and B. P. Sobolev, "CaF_2-BaF_2 phase diagram," Dokl. Phys. Chem. **401**(4-6), 53–55. Nauka/Interperiodica (2005).
18. P. A. Popov, A. A. Krugovykh, V. A. Konyushkin, A. N. Nakladov, S. V. Kuznetsov, and P. P. Fedorov, "Thermal Conductivity of $Sr_{1-x}Ba_xF_2$ Single Crystals," Inorg. Mater. **57**(6), 629–633 (2021).
19. D. Klimm, M. Rabe, R. Bertram, R. Uecker, and L. Parthier, "Phase diagram analysis and crystal growth of solid solutions $Ca_{1-x}Sr_xF_2$," J. Cryst. Growth **310**(1), 152–155 (2008).
20. R. H. Nafziger, "High-Temperature Phase Relations in the System BaF_2-SrF_2," J. Am. Ceram. Soc. **54**(9), 467 (1971).
21. J. L. Doualan, P. Camy, A. Benayad, V. Ménard, R. Moncorgé, J. Boudeile, F. Druon, F. Balembois, and P. Georges, "Yb^{3+} doped $(Ca,Sr,Ba)F_2$ for high power laser applications," Laser Phys. **20**(2), 533–536 (2010).
22. K. Veselský, J. Šulc, H. Jelínková, M. E. Doroshenko, V. A. Konyushkin, and A. N. Nakladov, "Spectroscopic and laser properties of a broadly tunable diode-pumped Tm^{3+}:CaF_2–SrF_2 laser," Laser Phys. Lett. **17**(2), 025802 (2020).
23. J. Liu, X. Feng, X. Fan, Z. Zhang, B. Zhang, J. Liu, and L. Su, "Efficient continuous-wave and passive Q-switched mode-locked Er^{3+}:CaF_2–SrF_2 lasers in the mid-infrared region," Opt. Lett. **43**(10), 2418–2421 (2018).
24. B. J. Dinerman and P. F. Moulton, "3-µm cw laser operations in erbium-doped YSGG, GGG, and YAG," Opt. Lett. **19**(15), 1143–1145 (1994).
25. G. A. Newburgh and M. Dubinskii, "Power and efficiency scaling of Er:ZBLAN fiber laser," Laser Phys. Lett. **18**(9), 095102 (2021).
26. L. Basyrova, P. Loiko, J. L. Doualan, A. Benayad, A. Braud, B. Viana, and P. Camy, "Thermal lensing, heat loading and power scaling of mid-infrared Er:CaF_2 lasers," Opt. Express **30**(5), 8092–8103 (2022).
27. M. Zong, Y. Wang, Z. Zhang, J. Liu, L. Zhao, J. Liu, and L. Su, "High-power 2.8 µm lasing in a lightly-doped Er: CaF_2 crystal," J. Lumin. **250**, 119089 (2022).
28. R. Švejkar, J. Šulc, H. Jelínková, V. Kubeček, W. Ma, D. Jiang, Q. Wu, and L. Su, "Diode-pumped Er:SrF_2 laser tunable at 2.7 µm," Opt. Mater. Express **8**(4), 1025–1030 (2018).
29. J. Šulc, M. Němec, R. Švejkar, H. Jelínková, M. E. Doroshenko, P. P. Fedorov, and V. V. Osiko, "Diode-pumped Er:CaF_2 ceramic 2.7 µm tunable laser," Opt. Lett. **38**(17), 3406–3409 (2013).
30. J. P. Russell, "The Raman spectrum of calcium fluoride," Proc. Phys. Soc. **85**(1), 194–199-2 (1965).
31. L. Su, J. Xu, W. Yang, X. Jiang, and Y. Dong, "Raman spectra of undoped and uranium doped CaF_2 single crystals," Chin. Opt. Lett. **3**(4), 219–221 (2005).

32. R. K. Chang, B. Lacina, and P. S. Pershan, "Raman scattering from mixed crystals $(Ca_xSr_{1-x})F_2$ and $(Sr_xBa_{1-x})F_2$," Phys. Rev. Lett. **17**(14), 755–758 (1966).
33. A. Ubaldini and M. M. Carnasciali, "Raman characterisation of powder of cubic RE_2O_3 (RE = Nd, Gd, Dy, Tm, and Lu), Sc_2O_3 and Y_2O_3," J. Alloys Compd. **454**(1-2), 374–378 (2008).
34. W. T. Carnall, P. R. Fields, and K. Rajnak, "Electronic energy levels in the trivalent lanthanide aquo ions. I. Pr^{3+}, Nd^{3+}, Pm^{3+}, Sm^{3+}, Dy^{3+}, Ho^{3+}, Er^{3+}, and Tm^{3+}," J. Chem. Phys. **49**(10), 4424–4442 (1968).
35. S. Normani, "Nd,Lu:CaF_2 for high-energy lasers" (Doctoral dissertation, Normandie Université) (2017).
36. B. R. Judd, "Optical Absorption Intensities of Rare-Earth Ions," Phys. Rev. **127**(3), 750–761 (1962).
37. G. S. Ofelt, "Intensities of Crystal Spectra of Rare-Earth Ions," J. Chem. Phys. **37**(3), 511–520 (1962).
38. P. A. Tanner, V. R. K. Kumar, C. K. Jayasankar, and M. F. Reid, "Analysis of spectral data and comparative energy level parametrizations for Ln^{3+} in cubic elpasolite crystals," J. Alloys Compd. **215**(1-2), 349–370 (1994).
39. B. Aull and H. Jenssen, "Vibronic interactions in Nd:YAG resulting in nonreciprocity of absorption and stimulated emission cross sections," IEEE J. Quantum Electron. **18**(5), 925–930 (1982).
40. J. B. Fenn Jr, J. C. Wright, and F. K. Fong, "Optical study of ion-defect clustering in CaF_2: Er^{3+}," J. Chem. Phys. **59**(10), 5591–5599 (1973).
41. D. R. Tallant and J. C. Wright, "Selective laser excitation of charge compensated sites in CaF_2: Er^{3+}," J. Chem. Phys. **63**(5), 2074–2085 (1975).
42. D. S. Moore and J. C. Wright, "Laser spectroscopy of defect chemistry in CaF_2: Er^{3+}," J. Chem. Phys. **74**(3), 1626–1636 (1981).
43. A. E. Nikiforov, A. Y. Zakharov, M. Y. Ugryumov, S. A. Kazanskii, A. I. Ryskin, and G. S. Shakurov, "Crystal fields of hexameric rare-earth clusters in fluorites," Phys. Solid State **47**(8), 1431–1435 (2005).
44. S. Normani, L. Basyrova, P. Loiko, A. Benayad, A. Braud, A. Hideur, and P. Camy, "Mid-infrared laser operation of Er^{3+}-doped BaF_2 and (Sr,Ba)F_2 crystals," Opt. Lett. **48**(2), 431–434 (2023).